

# To Be Decided

André Costa Batista, Ricardo Adriano, and Lucas S. Batista

**Abstract**—To be written.

**Index Terms**—Keyword 1, keyword 2, keyword 3. **Remember:** alphabetical order.

## I. INTRODUCTION

HERE we go.

## II. PROBLEM STATEMENT

Let  $D \in \mathbb{R}^2$  denote the Domain of Interest (DOI) embedded within a homogeneous, isotropic, nonmagnetic ( $\mu = \mu_0 = 4\pi \times 10^{-7}$  H/m), and lossless ( $\sigma = \sigma_0 = 0$  S/m) background medium with permittivity  $\epsilon_b = \epsilon_{rb}\epsilon_0$ , where  $\epsilon_0 \approx 8.85 \times 10^{-12}$  F/m. We consider a 2D Transverse Magnetic (TMz) polarization where the DOI is illuminated by incident plane waves and assume the time convention  $e^{j\omega t}$ . All scatterers are located within the DOI, and the scattered field  $E_z^s$  at point  $\rho \in S$  outside  $D$  is evaluated according to the following integral equation [1]:

$$E_z^s(\rho) = -\frac{k_b^2}{4} \int_D H_0^{(2)}(k_b|\rho - \rho'|) \chi(\rho') E_z(\rho') dS' \quad (1)$$

where  $k_b = \omega\sqrt{\epsilon_b\mu_0} = 2\pi/\lambda_b$  is the background wave number,  $\lambda_b$  is the wavelength of the incident wave,  $H_0^{(2)}$  is the zero-order Hankel function of the second kind,  $E_z$  is the total electric field in the DOI, and  $\chi$  is the contrast function given by

$$\chi(\rho) = \frac{\epsilon_r(\rho)}{\epsilon_{rb}} - 1 - j \frac{\sigma(\rho)}{\omega\epsilon_b}, \quad (2)$$

which maps the relative permittivity  $\epsilon_r(\rho)$  and conductivity  $\sigma(\rho)$  distributions within  $D$ . It should be noted that the term  $(-jk_b^2/4)H_0^{(2)}(k_b|\rho - \rho'|)$  corresponds to the Green's function in free space.

In electromagnetic inverse scattering problems, we aim to recover the contrast function  $\chi$  using a set of  $N_M$  measurements of the scattered field collected for each of the  $N_S$  sources. Additionally,  $E_z$  is also unknown in  $D$  and must be solved. For our formulation, the  $N_S$  sources correspond to  $N_S$  incidence angles of the plane wave, and the  $N_M$  measurements are taken at  $N_M$  points in  $S$ , arranged in a circular, equidistant array situated far from the center of the DOI by a radius

$R_O$ . By discretizing the DOI into  $N_X \times N_Y = N$  pixels, the inverse problem is solved numerically according to the following equation:

$$E_{ms}^s = - \sum_{n=1}^N G_{mn}^S \chi_n E_{ns} \quad (3)$$

where  $G^S$  is given according to the Richmond discretization [2], [3]. Equation (3) can also be expressed in matrix form:

$$\mathbf{E}^S = \mathbf{G}^S \chi \mathbf{E} \quad (4)$$

where  $\mathbf{E}^S$  is the  $N_M \times N_S$  scattered field matrix,  $\mathbf{G}^S$  is the  $N_M \times N$  Green's function matrix,  $\chi$  is the  $N \times N$  contrast diagonal matrix, and  $\mathbf{E}$  is the  $N \times N_S$  total electric field matrix.

It is important to highlight that, although assumptions are made regarding the scattered field domain and the incident field, the proposed indicators do not depend on these assumptions. They can be applied in any scenario where these entities are defined, and the assumptions in this paper serve only to clearly establish the context in which the indicators are tested.

## III. INDICATORS

Once the result of the contrast function reconstruction is obtained by a given algorithm, the error in recovering the shape and location of the objects can be measured by comparing it with the original images. This means that the application of these metrics is relevant in studies where the exact response is known. Although in many real-world scenarios the imaged scatterer is unknown, applying these metrics to known cases can be valuable for comparing the performance of different algorithms and for estimating a confidence interval for the average performance of an algorithm in a given configuration. Therefore, these metrics are relevant tools that can contribute to the investigation and evaluation of algorithms for the problem.

For the two indicators that will be explained below, the image of the original contrast function of the problem and the image reconstructed by any algorithm will be denoted by the matrices  $\bar{\chi}_o$  and  $\bar{\chi}_r$ , both of size  $N_X \times N_Y$ . In other words, the elements of these matrices represent the pixels of the images.

### A. Shape Error

The contrast function has complex values when the medium or the scatterers have losses. Therefore, the first step is to account for the possibility that the elements of the matrices  $\bar{\chi}_o$  and  $\bar{\chi}_r$  have real and imaginary parts. The simplest approach is to use the magnitude of the complex variables as the value of each pixel. This choice does not eliminate the possibility that objects with different contrasts might have

This work has been supported by the Brazilian agencies Coordination for the Improvement of Higher Education Personnel - Brazil (CAPES) through the Academic Excellence Program (PROEX) under Grant 88887.815891/2023-00, FAPEMIG (Research Support Foundation of the State of Minas Gerais), and CNPq (The National Council for Scientific and Technological Development).

A. C. Batista, R. Adriano, and L. S. Batista are with the Department of Electrical Engineering, Universidade Federal de Minas Gerais, Belo Horizonte, MG 31270-901, Brazil (e-mail: andre-costa@ufmg.br; rluiz@ufmg.br; lusoba@ufmg.br). A. C. Batista and L. S. Batista are also with Operations Research and Complex Systems Laboratory (ORCS Lab), Belo Horizonte, MG, Brazil.

the same magnitude. However, in cases involving only lossless materials, this approach is not problematic because the contrast is purely real. Since the primary objective is to verify the shape of the scatterers, the critical aspect is distinguishing between the background medium and the scatterer, with the background medium having zero contrast. Thus, this approach to simplifying the methodology for measuring shape error should not have significant consequences in performance verification scenarios for the algorithm.

The contrast function reconstructed by many algorithms – such as BIM, DBIM, CSI, SOM, among others – is commonly a discretized approximation of a continuous surface. Therefore, even if the original image contains only objects with well-defined boundaries and homogeneous contrast, the image of these objects obtained by the algorithms will have frequently smooth edges, i.e., the contrast value gradually varies between the background medium and the object's value. Consequently, identifying a contour in the resulting image is heuristic because it requires selecting a criterion to define the contrast value at which a pixel can be considered as belonging to the object. For simplicity, the threshold  $T$  for considering a pixel in the recovered image to be within an object's contour will be defined as half of the total contrast variation in the image, i.e.:

$$T = \min(|\bar{\chi}_r|) + \frac{1}{2} [\max(|\bar{\chi}_r|) - \min(|\bar{\chi}_r|)] \quad (5)$$

This approach has advantages and disadvantages. If the reconstructed image contains multiple scatterers, and one or more of them has a contrast below this threshold, the methodology will fail to detect the contour of these objects. However, in scenarios where there is only one scatterer in the image, this approach is simple and effective. In fact, a single scatterer is the most objective way to test an algorithm's potential in recovering geometry, since the presence of multiple scatterers can degrade the algorithm's performance due to the influence of the induced currents in each scatterer on the scattering of the other. Furthermore, this approach poses no issues for algorithms capable of accurately capturing contours, such as machine learning-based methods. Moreover, instead of using the values from the original image, it is more beneficial to use only the values from the reconstructed image, both to isolate the influence of error in the contrast estimate and to apply the metric to qualitative methods that do not estimate contrast. If, for some reason, the original contrast function involves soft boundaries of the objects, the threshold might also be applied to the original image.

Once the thresholding step is applied, the contours of the scatterers can be determined. One of the techniques suitable for this task is the Marching Squares algorithm [4]. This algorithm efficiently returns a set of points that delineate each contour. It is important to note that hollow objects may have two or more contours. Additionally, if the imaging algorithm fails to detect an object, a discrepancy will arise in the number of contours between the original and reconstructed images.

For these reasons, instead of comparing the geometries through calculations based on the points of each contour, we prefer to perform the comparison based on the number of

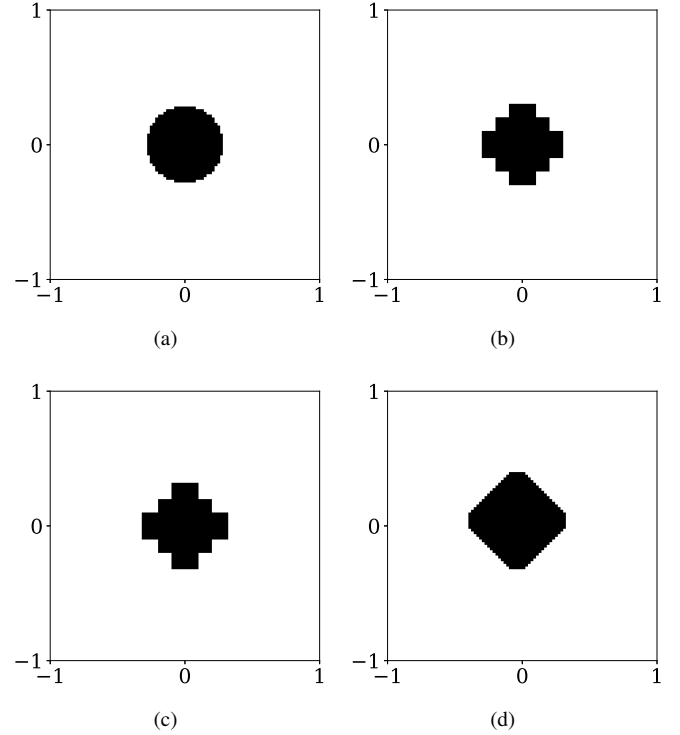


Fig. 1. An example illustrating the differences between nearest neighbor interpolation and the adopted contour detection methodology. (a) Original image of the scatterer (resolution 100x100); (b) Image reconstructed by an imaging algorithm after thresholding (20x20); (c) Image reconstructed to the original resolution using nearest neighbor interpolation; (d) Image reconstructed to the original resolution using contour identification.

pixels that were misclassified. Specifically, after identifying which pixels fall within each contour in each image, we can determine which pixels belonged to the scatterers in the original image but were not captured in the reconstructed image (false negatives) and which pixels did not belong to the scatterers in the original image but were classified as such in the reconstructed image (false positives).

A potential question that may arise from this choice is why not directly calculate false positives and false negatives immediately after thresholding. One reason is that original and reconstructed images typically have different resolutions. While the nearest neighbor interpolation method is an alternative for addressing this issue, the chosen approach may be more effective for capturing and preserving object contours, particularly when the resolution of the reconstructed image is significantly lower. This is illustrated in Fig. 1.

The sum of false negatives and false positives can be easily obtained by applying the XOR operation between the two images. Then, we can compute the shape error as the ratio between the number of incorrectly classified pixels and the total number of pixels that are part of the scatterers in the original image. Additionally, if we consider the shape error in percentage values, we can then define the indicator  $\zeta_S$  as

$$\zeta_S = \frac{FP + FN}{TP} \times 100\%, \quad (6)$$

where FP and FN are the numbers of false-positive and false-negative pixels, respectively, and TP is the total number of

pixels that are part of the scatterers in the original image. Therefore, the indicator assumes values greater than or equal to zero. Note that values greater than 100% are also possible, indicating that the reconstructed image has more incorrectly classified pixels than the total number of pixels that make up the scatterers in the original image. This can occur more frequently when the number of pixels of the scatterer in the original image is small. The Algorithm 1 summarizes the steps for calculating the shape error indicator.

---

**Algorithm 1** Compute Shape Error Indicator  $\zeta_S$

---

**Require:** Original contrast distribution  $\chi_o$

**Require:** Reconstructed contrast distribution  $\chi_r$

**Require:** Threshold factor  $threshold = 0.5$  (default)

**Ensure:** Shape error indicator  $\zeta_S$  (%)

- 1: Extract magnitude information from both contrast distributions
  - 2: Determine adaptive threshold based on reconstructed image dynamic range
  - 3: Apply binary classification to identify object and background regions
  - 4: **if** no object regions detected in reconstruction **then**
  - 5:     **return** complete failure indicator (100%)
  - 6: **end if**
  - 7: Extract object boundaries using contour detection methodology
  - 8: Normalize spatial coordinates to handle resolution differences between images
  - 9: Generate binary masks from contour information using polygon filling:
  - 10:     - Apply odd-parity rule to determine interior points
  - 11:     - Handle multiple contours for complex geometries
  - 12: Compare geometric regions through symmetric difference operation
  - 13: Quantify classification errors relative to original object size
  - 14: **return** normalized shape error as percentage
- 

### B. Position Error

The methodology for calculating the position detection error shares similarities with that of shape error calculation. As it is done when computing the shape error, the position error calculation also uses the absolute value of the image contrasts and applies the same thresholding operation. The reasons for this approach are the same.

The key difference lies in the method of position error calculation, which is based on comparing the centroid of pixels classified as objects by the thresholding operation in each image. Specifically, the centroid for each image is determined by averaging the coordinates of the pixels that constitute the objects. This method does not require contour detection, as the coordinate points are within the same boundaries for both images, even when resolutions differ.

The position error indicator is then defined as the Euclidean distance between the centroids in the two images. It is important to note that these centroids are normalized within a

range of 0 to 1, where 0 represents the image's origin and 1 represents its end. By multiplying this distance by 100, the error can be interpreted as a percentage relative to the image size. Thus, the indicator quantifies the error in object localization relative to the image size, allowing its application across test sets with varying domain sizes. Therefore, the position error indicator  $\zeta_P$  is defined as:

$$\zeta_P = \sqrt{(x_c^R - x_c^O)^2 + (y_c^R - y_c^O)^2} \times 100\%, \quad (7)$$

where  $(x_c^R, y_c^R)$  and  $(x_c^O, y_c^O)$  are the centroids of the reconstructed and original images, respectively.

It should be noted that inaccuracies in the reconstructed geometry of objects can significantly influence the position error calculation. For example, if a star-shaped object with five points is reconstructed with one point distorted, this distortion will affect the object's centroid, thereby impacting the position error. However, this effect is expected, as any criterion for determining an object's position inherently considers the pixels defining it, as it is for its geometry. Furthermore, the proposed indicator is straightforward and versatile, applicable even in scenarios involving images with multiple objects. The Algorithm 2 summarizes the steps for calculating the position error indicator.

---

**Algorithm 2** Compute Position Error Indicator  $\zeta_P$

---

**Require:** Original contrast distribution  $\chi_o$

**Require:** Reconstructed contrast distribution  $\chi_r$

**Ensure:** Position error indicator  $\zeta_P$  (%)

- 1: Extract magnitude information from both contrast distributions
  - 2: Determine adaptive threshold based on reconstructed image dynamic range
  - 3: Generate binary object masks using threshold-based classification
  - 4:     - Original mask: pixels with non-zero contrast values
  - 5:     - Reconstructed mask: pixels above computed threshold
  - 6: **if** no object regions detected in reconstruction **then**
  - 7:     **return** complete failure indicator (100%)
  - 8: **end if**
  - 9: Create normalized coordinate systems for both images
  - 10:     - Map pixel coordinates to unit interval [0,1]
  - 11:     - Handle potential resolution differences
  - 12: Compute geometric centroids using weighted coordinate averaging:
  - 13:     - Calculate center of mass for original object mask
  - 14:     - Calculate center of mass for reconstructed object mask
  - 15: Measure centroid displacement using Euclidean distance metric
  - 16: Normalize distance to percentage scale relative to image dimensions
  - 17: **return** position error as percentage of maximum possible displacement
- 

## IV. COMPUTATIONAL EXPERIMENTS

The experiments presented in this article are intended to illustrate the application of the proposed indicators. The design

of these experiments focuses on demonstrating the potential utility of these indicators, rather than achieving pioneering results in the field. Nevertheless, the findings from these experiments can still provide a foundation for further research by the scientific community.

The experiments were conducted using the open-source library EISPY2D [5], specifically developed to design and evaluate algorithms for the inverse electromagnetic scattering problem. Both indicators will be analyzed, with each approach featuring two case studies (one fundamental and the other exploring a particular aspect) as well as a benchmarking study. The case studies aim to assess performance in specific scenarios, while the benchmarking study facilitates broader generalization of the results.

For all experiments, the following common parameters were used:  $\lambda_b = 1$  m, noise level = 5%, relative permittivity of the background medium  $\epsilon_{rb} = 1$ , and incident wave amplitude = 1 V/m. Data synthesis was performed using the MoM-CG-FFT algorithm [6] with 5000 iterations.

#### A. Shape Recovering Study

To evaluate shape error, two case studies were conducted. The first case study involves a single scatterer with homogeneous contrast, while the second case study involves a scatterer with variable contrast. These case studies were selected to demonstrate the application of the proposed indicator in typical scenarios encountered in electromagnetic scattering problems. Additionally, a benchmarking study was performed to assess the average performance of algorithms in more general situations.

In all instances, the dimensions of the DoI were set to  $2\lambda_b \times 2\lambda_b$ , and the measurement points' distance radius  $R_O$  was fixed at  $4\lambda_b$ .

1) *Single scatterer*: The first case study was designed to evaluate the applicability of the proposed indicator in a straightforward scenario where various algorithms could be applied. This case study features a scatterer shaped like a five-pointed star, centrally positioned within the image. This choice was made to select a geometry that, while symmetric and well-defined, has more vertices compared to more common shapes such as squares or triangles. The contrast was set to 0.25, and the radius from the center of the scatterer to the farthest vertices was set to  $0.9\lambda_b$ . A total of 80 measurement points ( $N_M$ ) and 80 incidence angles ( $N_S$ ) were used. Under these conditions, the Degree of Nonlinearity (DNL) for the test is 0.12, which is significantly lower than the threshold beyond which the Born Approximation becomes inapplicable, i.e., 1 [7]. The scattered field was synthesized using a discretization of  $120 \times 120$  pixels for the original image, and all reconstructions were performed using a discretization of  $40 \times 40$  pixels.

For this experiment, the following algorithms were considered: LSM, OSM, BIM, CSI, and SOM. Their parameters were chosen after empirical tests that aimed to achieve their best performance. The configurations for each algorithm are as follows:

- Linear Sampling Method (LSM):
  - Threshold: 0.7;

- Regularization Method: Conjugate Gradient with 300 iterations.
- Orthogonality Sampling Method (OSM):
  - Threshold: 0.35;
- Born Iterative Method (BIM):
  - Regularization Method: Conjugate Gradient with 300 iterations.
  - Stopping Criterion: 30 iterations.
- Contrast Source Inversion (CSI):
  - Stopping Criterion: 300 iterations.
- Subspace Optimization Method (SOM):
  - Stopping Criterion: 30 iterations.
  - Eigenvalue Cutoff Index: 5.

The images reconstructed by each algorithm are shown in Fig. 2. For the qualitative methods, OSM exhibited contrast variation within the object, which is consistent with the inherent characteristics of the method. Additionally, OSM recovered a larger area with more defined vertices compared to LSM. Regarding the quantitative methods, CSI demonstrated the lowest performance in recovering the object's contrast value close to the ground truth. Moreover, the quantitative methods produced more accurate contours than their qualitative counterparts.

Table I summarizes the results of the shape error indicator for each algorithm. The results indicate that BIM and SOM achieved the best performance, while CSI, LSM and OSM performed similarly. This is consistent with the observations from Fig. 2, since the quantitative methods had a greater ability to capture the object's contours compared to the qualitative methods. This was not true for CSI, which, due to its greater difficulty in quantifying the object's contrast, had more difficulty in capturing the object's contours.

TABLE I  
RESULTS FOR THE SINGLE SCATTERER CASE STUDY.

Method	LSM	OSM	BIM	CSI	SOM
$\zeta_S$ (%)	29.2	24.5	14.9	26.3	15.4

2) *Varying contrast*: Another type of study that can complement the analysis of algorithm performance in object geometry reconstruction is the observation of indicator performance with varying object contrast. Specifically, for a given scatterer, as its contrast value increases, the DNL increases, and consequently, algorithms may lose performance since the problem becomes more challenging. To demonstrate this relationship, the same scatterer from the previous study was considered with identical scenario configurations. The only modification was that the original image resolution was increased to  $160 \times 160$  pixels to ensure precision in field calculations for high contrast scenarios.

The scatterer was reconstructed using five contrast values: 0.25, 0.5, 0.75, 1.0, and 1.5. Fig. 4(b) shows the corresponding DNL for each contrast value. For this study, the OSM and SOM methods were employed with the same configurations as the previous study. While the method parameters could be optimized for each contrast value, they were kept constant across

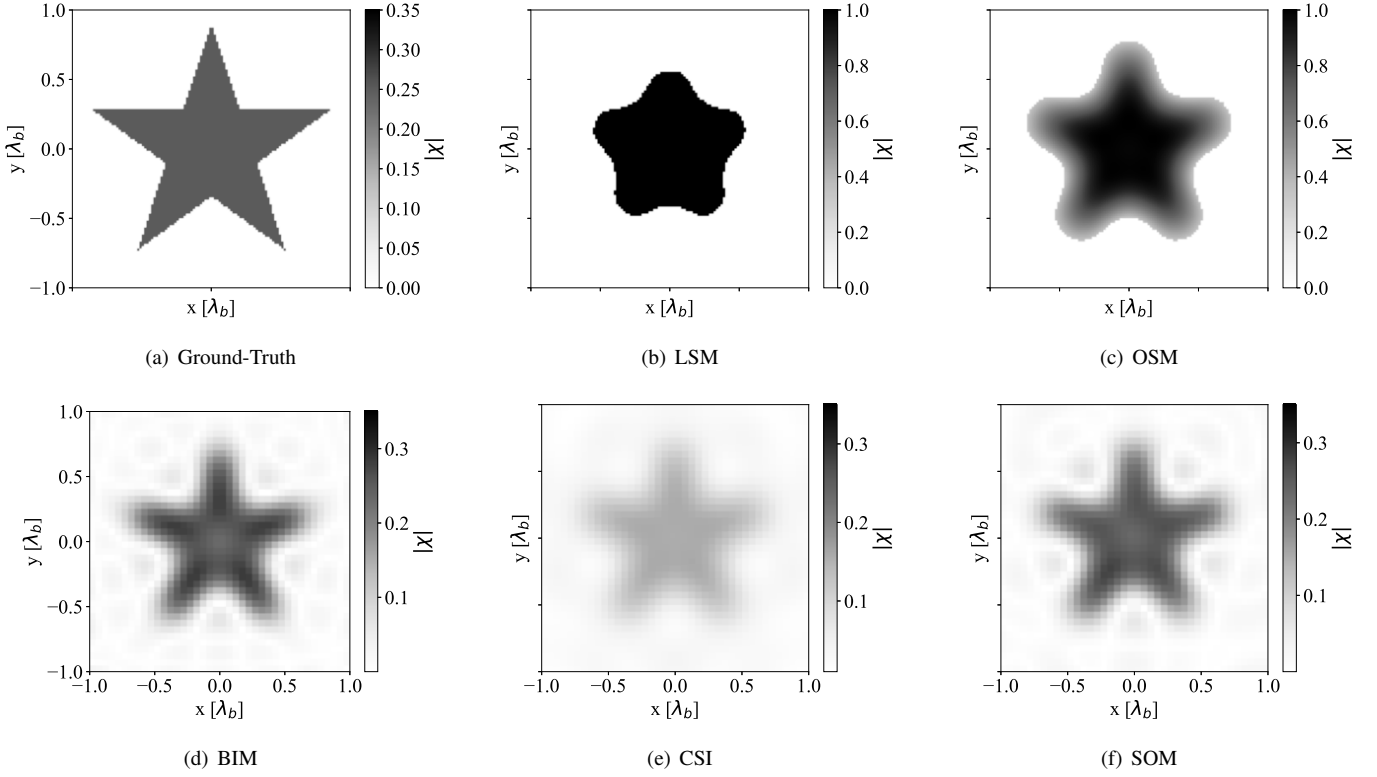


Fig. 2. Shape recovering study, single scatterer: ground-truth and reconstructed images by each algorithm.

all contrast values to demonstrate the indicator's applicability in a controlled manner.

**EU PRECISO RODAR NOVAMENTE O EXPERIMENTO PORQUE O NÚMERO DE MEDIÇÕES E FONTES NÃO FORAM IGUAIS NA PRIMEIRA VEZ.**

Fig. 3 shows the images reconstructed by OSM and SOM for each contrast value. As expected, reconstruction precision decreased with increasing contrast, reaching a point where the geometry was no longer correctly recovered for the highest contrast value (1.5), particularly in the case of SOM. Notably, SOM was able to estimate the scatterer's contrast with reasonable precision up to  $\chi = 1$ , where the DNL is approximately 2.

Fig. 4(a) presents the shape error indicator  $\zeta_S$  for both OSM and SOM methods. The results demonstrate that the shape error increases proportionally with contrast value, which is consistent with the expected algorithmic behavior. Furthermore, for  $\chi = 1.5$ , the indicator  $\zeta_S$  exceeds 100%, indicating that the number of incorrectly classified pixels surpasses the number of pixels composing the scatterer in the original image. This observation aligns with the finding that geometry recovery fails at this contrast level. Additionally, the difference between the OSM and SOM indicators remains relatively constant up to  $\chi = 1$ .

3) *Average performance:* When comparing multiple algorithms, it is advantageous to conduct case studies using test sets that represent specific problem classes. This approach enables the measurement and statistical comparison of average algorithm performance, thereby supporting more robust and reliable conclusions regarding their relative effectiveness.

Following such an approach, an experiment was conducted to compare the LSM, OSM, BIM, CSI, and SOM algorithms. This experiment utilized 30 scatterer images with varying geometries to provide a more comprehensive assessment of algorithm performance across different shape configurations.

The scatterers were randomly generated as polygons with 4 to 15 vertices, where the radius from the center to the farthest vertices ranged between  $0.45\lambda_b$  and  $0.9\lambda_b$ . The contrast was fixed at 0.25 for all scatterers, and the data synthesis parameters from Section IV-A1 were maintained for consistency.

Due to the geometric variations, the DNL for each instance varies accordingly, as illustrated in Fig. 5(a). The median DNL exceeds the value from the experiment in Section IV-A1, though both remain significantly below the threshold of 1, above which the Born Approximation becomes inapplicable [7]. This experimental design enables the assessment of statistical evidence supporting the superiority of any algorithm within this problem class.

Fig. 5(b) presents the shape error indicator  $\zeta_S$  for each algorithm across all test instances. The results reveal a clear performance distinction when considering LSM, which demonstrates significantly worse performance compared to the other methods. Among the remaining algorithms, while overall performance levels appear similar, some patterns emerge: CSI exhibits higher error rates across a significant number of instances, whereas BIM demonstrates superior performance in a significant portion of the test cases.

While Fig. 5(b) provides initial insights into the results, statistical testing is important to validate the conclusions rigorously. To this end, Randomized Complete Block Design

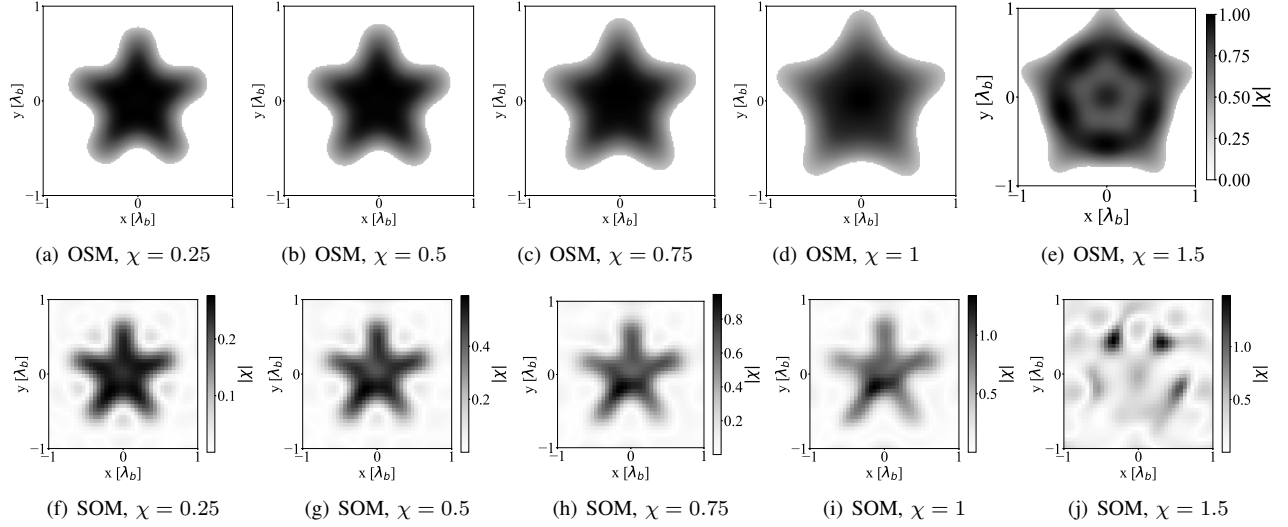


Fig. 3. Shape recovering study, varying contrast: reconstructed images by OSM and SOM for different contrast values.

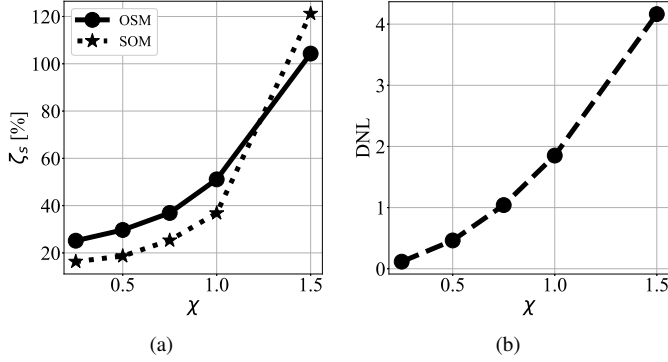
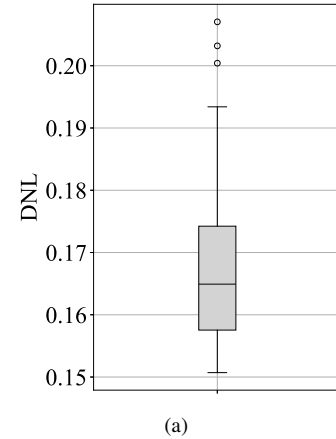


Fig. 4. Shape recovering study, varying contrast: (a) shape error indicator  $\zeta_S$  for OSM and SOM; (b) Degree of Nonlinearity (DNL) for each contrast value.

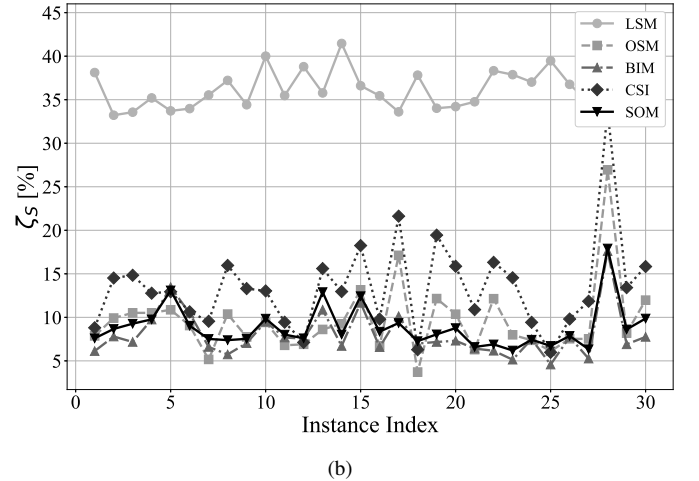
(RCBD) was applied to assess whether significant paired differences exist among the algorithms. RCBD is a statistical test which is used to evaluate significant paired differences between three or more related groups when the data meet the assumptions for parametric tests. In this context, the groups correspond to the algorithms, and the measurements are the  $\zeta_S$  indicator values for each algorithm across all instances. Given that LSM demonstrated substantially inferior performance compared to the other algorithms, it was excluded from the statistical analysis to focus on the more competitive methods.

After validating normality assumption, the p-value computed by RCBD result was less than  $10^{-15}$ , indicating that at least one pair of algorithms shows a significant mean paired difference. Subsequently, multiple paired T-Test with Bonferroni correction were applied to identify which algorithms have significant mean paired differences between them. The p-values obtained from these tests are presented in Table II. As shown in the table, the null hypothesis that algorithms have equal performance is rejected for all algorithm pairs, except for OSM-SOM, indicating that OSM and SOM do not exhibit a significant difference in their average performance.

To complement the analysis, Fig. 6 presents the 95%



(a)



(b)

Fig. 5. Shape recovering study, average performance: (a) Degree of Nonlinearity (DNL) for each scatterer; (b) shape error indicator  $\zeta_S$  for each algorithm in each instance.

confidence intervals for the mean paired differences of the shape error indicator  $\zeta_S$  for each algorithm pair. As observed, the differences consistently favor BIM, providing evidence for

TABLE II  
SHAPE RECOVERING STUDY, AVERAGE PERFORMANCE:  $p$ -VALUES FOR THE PAIRED T-TEST WITH BONFERRONI CORRECTION.

Pairs	OSM-BIM	OSM-CSI	OSM-SOM	BIM-CSI	BIM-SOM	CSI-SOM
$p$ -value	$< 10^{-2}$	$< 10^{-11}$	0.15	$< 10^{-7}$	$< 10^{-4}$	$< 10^{-6}$

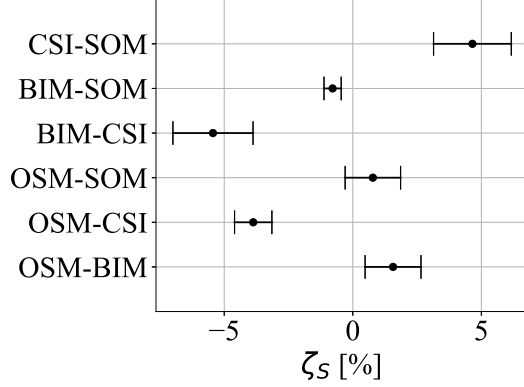


Fig. 6. Shape recovering study, average performance: Confidence intervals (95%) for the shape error indicator  $\zeta_S$  for each pair of algorithms.

BIM's superiority over the other algorithms. Additionally, CSI performs significantly worse than both BIM, OSM and SOM. However, all differences in average performance are less than 7%.

Furthermore, it is noteworthy that BIM also achieved the best performance in the study from Section IV-A1. However, while the difference between SOM and OSM was significant in the experiment from Section IV-A1, this benchmarking study provided evidence for performance equivalence between these two methods. In other words, if conclusions were drawn based solely on the case study, this could lead to a misconception about the performance of these two methods in this problem configuration. Therefore, this reinforces the importance of conducting benchmarking studies combined with statistical analyses to obtain more robust conclusions about algorithm performance.

### B. Position Detection Study

In many scenarios where algorithms can adequately reconstruct the geometry of scatterers, the error in detecting scatterer positions tends to be low. For example, in the study described in Section IV-A1, the  $\zeta_P$  indicator values obtained by LSM, OSM, BIM, CSI, and SOM were 0.049%, 0.057%, 0.25%, 0.31%, and 0.14%, respectively. This occurs because geometry and position are scatterer characteristics that algorithms typically do not handle separately.

An exception would be algorithms that solve the imaging problem as an optimization problem, where the decision variables are the position, vertices (or other characteristics of a predefined geometry), and contrast of the scatterers [?], [?], [?]. Additionally, in scenarios involving strong scatterers, traditional methods generally struggle to recover scatterer geometry effectively due to the increased problem hardness.

In such scenarios, studying position detection becomes more relevant.

Considering this, the experiments in this section were designed for scenarios involving strong scatterers, where traditional methods cannot adequately recover scatterer geometry. Therefore, the position error indicator  $\zeta_P$  serves as a relevant metric for comparing algorithm performance in such challenging scenarios.

- 1) *Single scatter:*
- 2) *Multiple scatterers:*
- 3) *Average performance:*

### C. Breast Phantom Study

## V. CONCLUSION

A conclusion section is not required. Although a conclusion may review the main points of the paper, do not replicate the abstract as the conclusion. A conclusion might elaborate on the importance of the work or suggest applications and extensions. [8]

## ACKNOWLEDGMENT

Use the singular heading even if you have many acknowledgments. In most cases, sponsor and financial support acknowledgments are placed in the unnumbered footnote on the first page, not here.

## REFERENCES

- [1] R. F. Harrington, *Time-Harmonic Electromagnetic Fields*. Wiley-IEEE Press, 2001.
- [2] J. Richmond, "Scattering by a dielectric cylinder of arbitrary cross section shape," *IEEE Transactions on Antennas and Propagation*, vol. 13, no. 3, pp. 334–341, 1965.
- [3] *The Electromagnetic Inverse Scattering Problem*. John Wiley & Sons, Ltd, 2010, ch. Three, pp. 20–56. [Online]. Available: <https://onlinelibrary.wiley.com/doi/abs/10.1002/9780470602492.ch3>
- [4] W. E. Lorensen and H. E. Cline, "Marching cubes: A high resolution 3d surface construction algorithm," in *Proceedings of the 14th Annual Conference on Computer Graphics and Interactive Techniques*, ser. SIGGRAPH '87. New York, NY, USA: Association for Computing Machinery, 1987, p. 163–169. [Online]. Available: <https://doi.org/10.1145/37401.37422>
- [5] A. Costa Batista, R. Adriano, and L. S. Batista, "Eispy2d: An open-source python library for the development and comparison of algorithms in two-dimensional electromagnetic inverse scattering problems," *IEEE Access*, vol. 13, pp. 92 134–92 154, 2025.
- [6] C.-C. Su, "Calculation of electromagnetic scattering from a dielectric cylinder using the conjugate gradient method and fft," *IEEE transactions on antennas and propagation*, vol. 35, no. 12, pp. 1418–1425, 1987.
- [7] O. M. Bucci, N. Cardace, L. Crocco, and T. Isernia, "Degree of non-linearity and a new solution procedure in scalar two-dimensional inverse scattering problems," *JOSA A*, vol. 18, no. 8, pp. 1832–1843, 2001.
- [8] X. Chen, *Computational methods for electromagnetic inverse scattering*. Wiley Online Library, 2018, vol. 244.